ACS Energy Letters

http://pubs.acs.org/journal/aelccp

LETTER

Ultrastable Anode Interface Achieved by Fluorinating Electrolytes for All-Solid-State Li Metal Batteries

Feipeng Zhao, Qian Sun, Chuang Yu, Shumin Zhang, Keegan Adair, Sizhe Wang, Yulong Liu, Yang Zhao, Jianwen Liang, Changhong Wang, Xiaona Li, Xia Li, Wei Xia, Ruying Li, Huan Huang, Li Zhang, Shangqian Zhao, Shigang Lu, and Xueliang Sun*

Cite This: *ACS Energy Lett.* 2020, 5, 1035−1043

Read Online

ABSTRACT: All-solid-state Li metal batteries (ASSLMBs) have attracted significant attention because of their high energy density and improved safety. However, the poor stability at the Li anode/solid-state electrolyte (SSE) interface is a long-standing problem that limits the current density and capacity, thus hindering the practical application of ASSLMBs. Herein, fluorination of an Argyrodite Li_6PS_5Cl (LPSCl) sulfide electrolyte is proposed to enhance the interfacial stability toward the Li metal anode. Because of the condensed and highly fluorinated interface that forms in situ with a self-healing essence, the Li metal symmetric cell employing the fluorinated LPSCl SSE enables ultrastable Li plating/stripping over 250 h at a superhigh current density of 6.37 mA cm^{-2} and a cutoff capacity of 5 mAh cm^{-2}. Furthermore, the Li metal treated by the fluorinated LPSCl SSE is demonstrated to deliver good durability and rate capability in full cells. Fluorinating sulfide electrolytes provides a new strategy for realizing high-performance ASSLMBs.

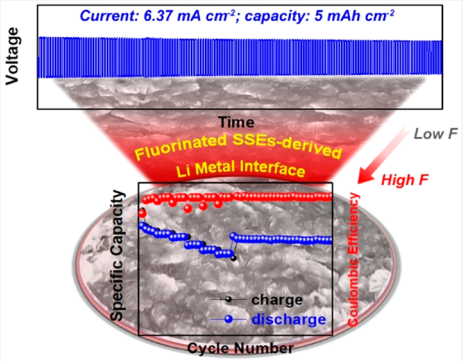

All-solid-state Li metal batteries (ASSLMBs) have been attracting an increasing amount of interest due to their high specific energy density and improved safety compared to those of conventional liquid-based Li-ion batteries (LIBs).[1−3] As one of the most important components of ASSLMBs, the solid-state electrolyte (SSE) plays a crucial role in the performance of ASSLMBs.[3−5] Over the past several decades, many studies have sought to improve the ionic conductivity of SSEs. Sulfide-based SSEs exhibit a very competitive ionic conductivity compared with those of the oxide- and polymer-based counterparts. In addition, sulfide-based SSEs can show a medium mechanical stiffness, intimate contact with electrode materials, and negligible grain boundary resistance.[6−9] Therefore, sulfide-based SSEs are viewed as one of the most promising SSE candidates for the commercialization of high-performance ASSLMBs.[10,11]

However, the poor compatibility at the Li anode and sulfide SSE interface is one of the major problems with sulfide-based ASSLMBs.[11,12] The following issues need to be addressed at the Li metal/SSE interface. (1) The reactivity between Li and sulfide SSEs is high.[13,14] Sulfide SSEs can be easily reduced by Li metal and decompose to form a passivation layer. The uncontrollable growth of the passivated layer can increase the interface impedance with continued cycling, eventually leading to the degradation of performance. (2) Li dendrites form through the grain boundary or voids in sulfide SSEs.[15,16] Electrons are inclined to accumulate on the grain boundary, which facilitates dendrite growth and propagation. Consequently, Li dendrites grow along the grain boundaries or voids of the SSE resulting from the inherent loose tap density. This would eventually lead to internal short circuits and battery failure.

Surface modification of the Li anode can effectively prevent the interfacial side reactions and Li dendrites growth to some extent.[17−20] Both F- and I-containing Li surfaces obtained by pretreating Li metal with various chemicals have been reported to be effective in reducing the interface impedance and hindering the formation of Li dendrites. However, the relatively low plating/stripping current density and capacity at room temperature (RT) (<0.5 mA cm^{-2} and <0.5 mAh

Received: January 29, 2020
Accepted: March 5, 2020
Published: March 5, 2020

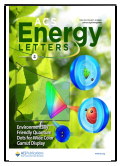

https://dx.doi.org/10.1021/acsenergylett.0c00207
ACS Energy Lett. 2020, 5, 1035−1043

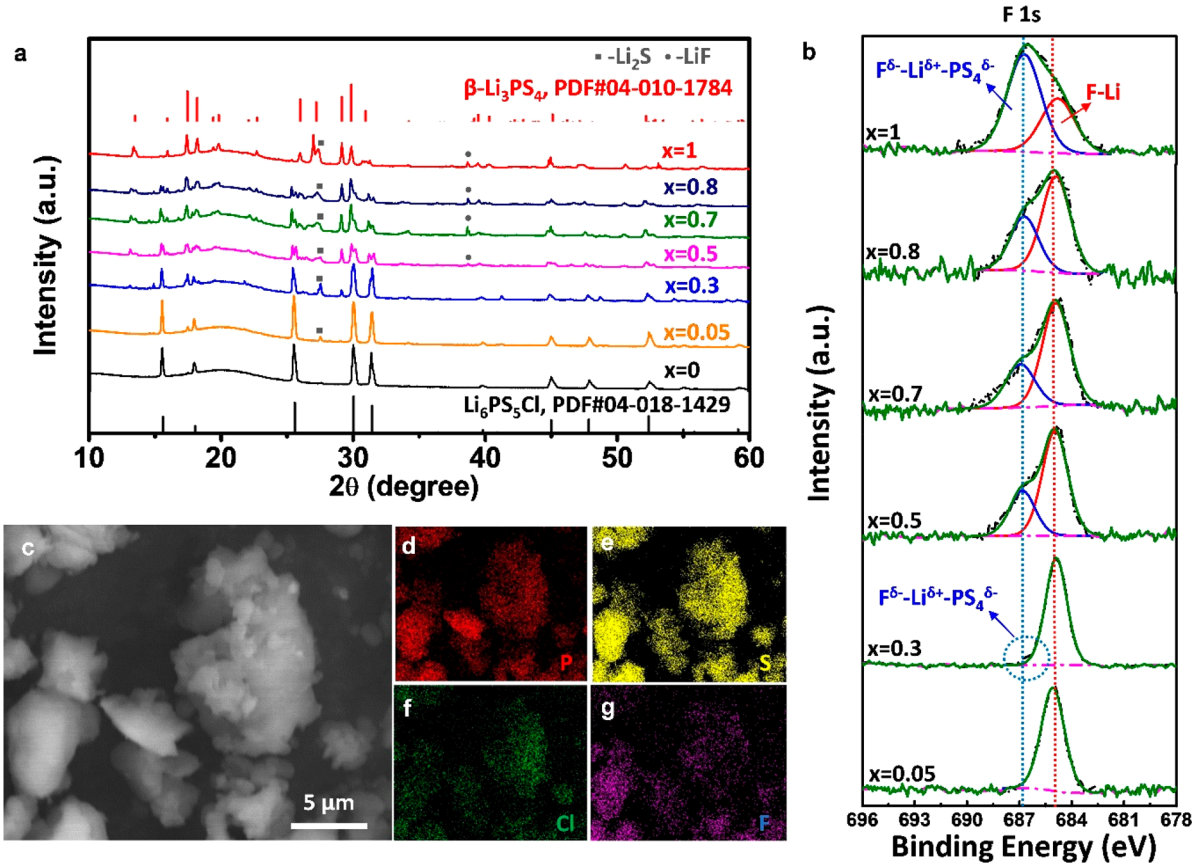

Figure 1. Characterizations of fluorinated sulfide-based SSEs. (a) XRD patterns of the prepared $LPSCl_{1-x}F_x$ sulfide-based electrolytes (x = 0, 0.05, 0.3, 0.5, 0.7, 0.8, and 1). (b) XPS spectra of F 1s in $LPSCl_{1-x}F_x$ sulfide-based electrolytes (x = 0.05, 0.3, 0.5, 0.7, 0.8, and 1). (c) SEM image of the $LPSCl_{0.3}F_{0.7}$ electrolyte. (d−g) EDX element mapping of the observed area of panel c.

cm^{-2}, respectively) limit their applications in high-rate ASSLMBs. On the other hand, LPS-based (Li_3PS_4) SSEs incorporated with LiI additives can show significantly improved capabilities (1 mA cm^{-2} and 1 mAh cm^{-2}, respectively, at RT) in suppressing Li dendrites at the Li/LPS-LiI interface.[21] The LiI-containing solid electrolyte interphase (SEI) layer can provide a favorable Li^+-ion conductivity and enable a homogeneous Li deposition. Nevertheless, considering the requirement for the practical application of ASSLBs, these previously reported strategies are still insufficient to meet the high current densities and cutoff capacities required to compete with state-of-the-art LIBs based on liquid electrolytes.[22]

LiF is a very popular compound that is widely employed as an essential component in stabilizing the SEI layer.[23−26] Additionally, it is reported that compared with the strategy that is developed on the surface treatment of Li metal, the other one based on modifying SSEs exhibits better protection for the Li metal. This is attributed to the self-healing feature of the SEI layer that forms in situ between the electrolyte and Li metal during cycling.[27,28] However, to the best of our knowledge, using F-containing SSEs to derive the formation of functional SEI layers with high concentration of LiF has rarely been reported. Herein, the concept that fluorinating the sulfide-based SSEs can induce the formation of a highly fluorinated Li anode interface is proposed. We take Argyrodite Li_6PS_5Cl (LPSCl) SSE as the host material and successfully incorporate F by replacing LiCl with various contents of LiF in the precursors to synthesize fluorinated $LPSCl_{1-x}F_x$ sulfide SSEs (x = 0.05, 0.3, 0.5, 0.7, 0.8, and 1). The Li symmetric cell using the optimized "$LPSCl_{0.3}F_{0.7}$" SSE can deliver an ultrastable Li plating and stripping for >250 h at a rarely reported current density of 6.37 mA cm^{-2} and a specific capacity of 5 mAh cm^{-2} at RT. This performance can be even comparable to the best performances in the liquid electrolyte counterparts. The in situ-formed interface between the Li metal and $LPSCl_{0.3}F_{0.7}$ SSEs possesses a dense morphology and shows a high concentration of LiF, playing a crucial role in achieving the high performance. In addition, when the high-quality Li anode interface is applied to the full cell, very promising cycling stability and rate performance are achieved at RT.

Using the conventional solid-state reaction method, various amounts of LiF were employed as one of the Li−halogen starting materials in replacement of LiCl to prepare a series of fluorinated $LPSCl_{1-x}F_x$ sulfide-based SSEs with different contents of incorporated F (see the detail in the Experimental Section of the Supporting Information). X-ray diffraction (XRD) measurements were conducted in an air-sensitive sample holder for the prepared SSEs. The evolution of the phase composition in the final products with different amounts of incorporated F is displayed in Figure 1a. It is noted that the broad diffraction peak at ∼19° is caused by the background from the Kapton film used on the holder, and the additional diffraction peak at ∼27.0° is assigned to the trace of Li_2S raw materials (PDF Card No. 00-026-1188). When x = 0, the product is the pure Argyrodite Li_6PS_5Cl electrolyte, and the corresponding diffraction peaks are consistent with the standard LPSCl pattern indexed as PDF Card No. 04-018-

https://dx.doi.org/10.1021/acsenergylett.0c00207
ACS Energy Lett. 2020, 5, 1035−1043

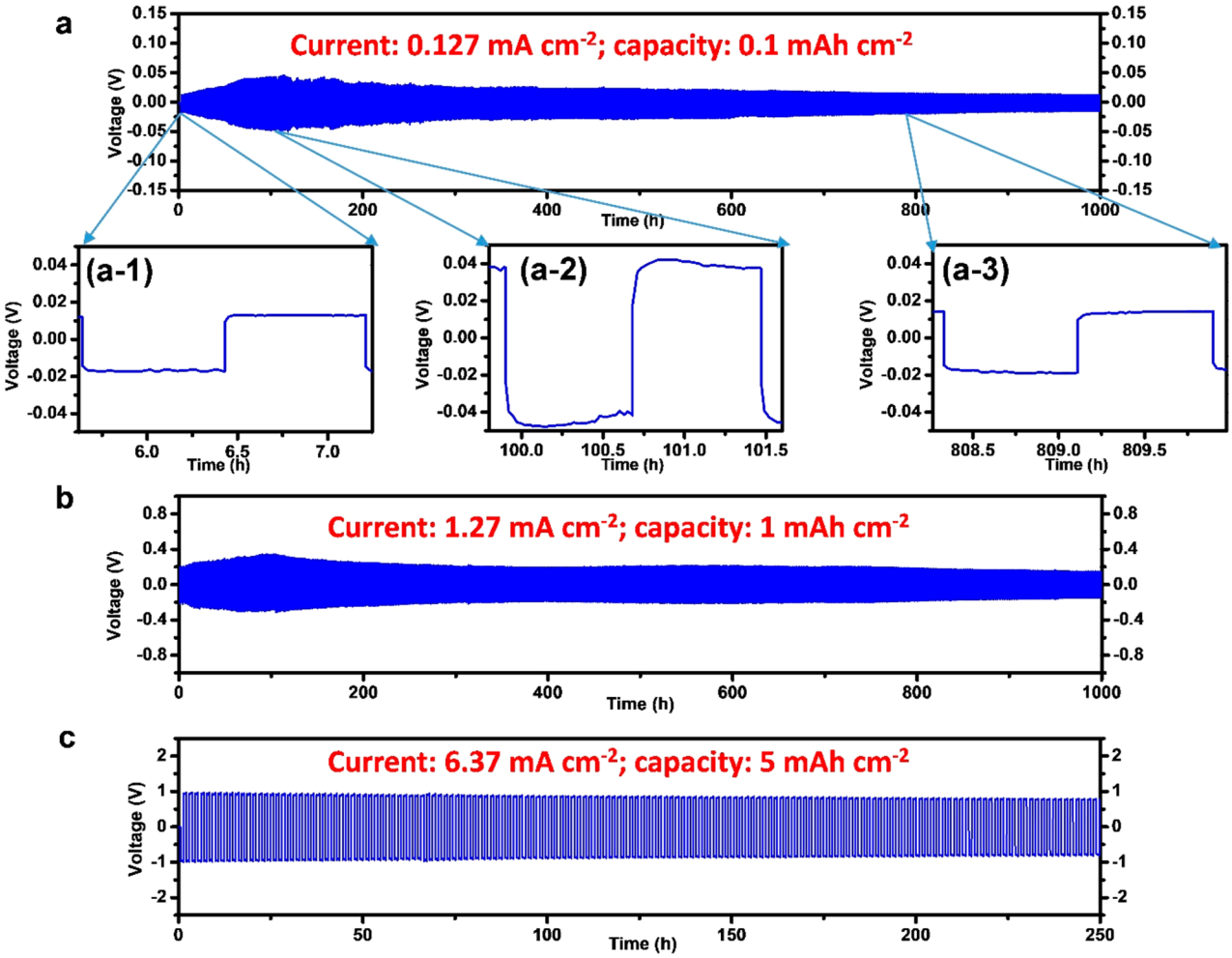

Figure 2. Li plating and stripping in Li//$LPSCl_{0.3}F_{0.7}$//Li symmetric cells. (a) Current density (0.127 mA cm^{-2}) and cutoff capacity (0.1 mAh cm^{-2}). (a-1−a-3) Magnified portions of panel a. (b) Current density (1.27 mA cm^{-2}) and cutoff capacity (1 mAh cm^{-2}). (c) Current density (6.37 mA cm^{-2}) and cutoff capacity (5 mAh cm^{-2}).

1429.[29] With the degree of fluorination of LPSCl-based electrolytes increasing, phase transformation from LPSCl to β-Li_3PS_4 is observed. The intensity of characteristic diffraction peaks belonging to the Li_6PS_5Cl phase decreases continuously, while the characteristic peaks of the β-Li_3PS_4 phase (PDF Card No. 04-010-1784) become apparent gradually. Diffraction peaks belonging to LiF can be observed after x = 0.5, which can be attributed to the excessive LiF precursor existing after F is completely incorporated into the LPSCl structure. The excessive LiF can fill in the boundary/pore of the SSEs, which can reduce the electronic conductivity and enhance the rigidity of the SSEs to suppress the penetration of Li dendrites.[30] X-ray photoelectron spectroscopy (XPS) was then employed to analyze the element chemical environment of the introduced F in the fluorinated $LPSCl_{1-x}F_x$ sulfide SSEs. As shown in Figure 1b, once x reaches 30, an obvious peak at 686.7 eV can be observed. This is ascribed to the interaction between F and PS_4^{3-} molecules, which can be expressed as "$F^{\delta-}$-$Li^{\delta+}$-$PS_4^{\delta-}$".[31] The existing peaks at 684.9 eV suggest the existence of Li−F bonds in the prepared $LPSCl_{1-x}F_x$ sulfide SSEs.[18] The corresponding change for S 2p and P 2p spectra can be observed in Figure S1. The characteristic peaks shift to a higher binding energy, confirming the electron cloud around S and P becomes weak after F incorporation. Raman spectra of the series of fluorinated $LPSCl_{1-x}F_x$ (x = 0, 0.5, 0.7, 0.8, and 1) sulfide-based SSEs (Figure S2) also verify that F incorporation can cause a red shift of the P−S symmetric stretching of PS_4^{3-} fingerprint ions (at ∼425 cm^{-1}),[32,33] indicating a strong electronegativity effect of F elements toward the PS_4^{3-} molecules. However, further detailed structure information will need to be acquired in future studies. The morphology of the prepared $LPSCl_{0.3}F_{0.7}$ electrolyte was studied using scanning electron microscopy (SEM). Similar to other reported lithium Argyrodite SSEs,[29,34] the $LPSCl_{0.3}F_{0.7}$ electrolyte shows irregular particles with a microlevel size (Figure 1c). Energy dispersive spectroscopy (EDS) element mapping (Figure 1d−g) for the selected area demonstrates that elements P, S, Cl, and F are homogeneously distributed. Electrochemical impedance spectroscopy (EIS) was employed to derive the ionic conductivity of prepared $LPSCl_{1-x}F_x$ electrolytes. As shown in Figure S3, the ionic conductivity decreases with an increase in F content at RT. The ionic conductivity of pure LPSCl electrolytes at RT reaches 3.1 × 10^{-3} S cm^{-1}, which agrees well with the published results.[35] When F is fully introduced (x = 1) into the electrolyte, the ionic conductivity drops to 5.2 × 10^{-4} S cm^{-1}. This ionic conductivity falls right at the level of LPS-based (β-Li_3PS_4) electrolytes. This evolution trend reflects the fact that F incorporated into the Argyrodite LPSCl phase can induce the gradual formation of a β-Li_3PS_4 conductive phase. Direct

https://dx.doi.org/10.1021/acsenergylett.0c00207
ACS Energy Lett. 2020, 5, 1035−1043

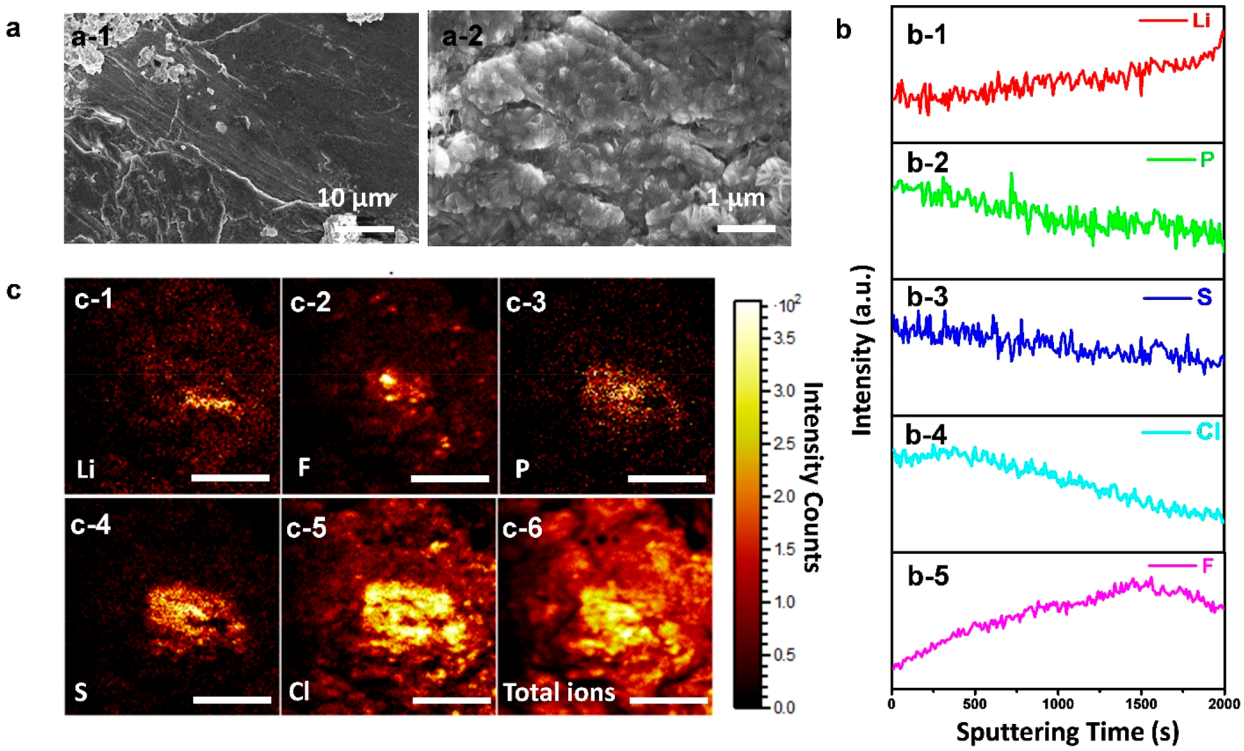

Figure 3. Characterizations of Li metal after cycling in the symmetric cells. (a) SEM images of the Li metal surface morphology. (b) ToF-SIMS depth profiles of each element on the Li metal. (c) Chemical species images on the Li metal after sputtering with a Cs^+-ion beam during the ToF-SIMS measurement. The scar bar is 200 μm.

current (dc) polarization measurements (Figure S4) were conducted to determine that the electronic conductivity of one representative composition, $LPSCl_{0.3}F_{0.7}$ SSEs, is approximately 9.85×10^{-10} S cm^{-1}, which is lower than that of the LPSCl SSEs (6.81×10^{-9} S cm^{-1}). The lower electronic conductivity is favorable and can restrict the formation of Li dendrites at the Li/SSE interface, as demonstrated recently by Han et al.[36]

The interface stability between Li metal and fluorinated $LPSCl_{1-x}F_x$ sulfide SSEs was then carefully evaluated through cycling Li−Li symmetrical cells under various current densities and cutoff capacities. As demonstrated in Figure S5, because the Li dendrite grows arbitrarily through the SSE, short circuits quickly occur in the symmetric cells with pure LPSCl and pure β-Li_3PS_4 electrolytes.[16,37] $LPSCl_{1-x}F_x$ electrolytes with a low degree of fluorination (x = 0.05, 0.3, and 0.5) cannot effectively prevent the short circuit caused by dendrite growth, while a high degree of fluorination (x = 0.8 and 1) can cause large overpotentials because of the lower ionic conductivity of the SSEs and thicker fluorinated interphase formed during plating/stripping. By contrast, x = 70 is found to be the optimized condition for guaranteeing a stable Li/$LPSCl_{0.3}F_{0.7}$ interface, with a limited overpotential and long cycling durability. As shown in Figure 2a, under a moderate plating/stripping condition of 0.127 mA cm^{-2} and 0.1 mAh cm^{-2}, the initial overpotential is around 15 mV (Figure 2a-1). This value is approximately 3 times larger than that for plating/stripping of Li in pure LPSCl electrolyte-based Li−Li symmetric cells, which is ascribed to the lower ionic conductivity of $LPSCl_{0.3}F_{0.7}$ electrolytes (7.1×10^{-4} S cm^{-1} at RT). With the initial activation process, a stable Li/$LPSCl_{0.3}F_{0.7}$ interface starts to form, and the overpotential reaches a maximum of 40 mV (Figure 2a-2). This in situ-formed Li/$LPSCl_{0.3}F_{0.7}$ interphase is robust and can prevent further side reactions and Li dendrite formation. Even after 1000 h, the Li//$LPSCl_{0.3}F_{0.7}$//Li symmetric cell remains stable and shows a very stable overpotential that recovers to the initial state at around 17 mV (Figure 2a-3). Time-resolved EIS profiles (Figure S6) were recorded for the Li/$LPSCl_{0.3}F_{0.7}$ interfacial impendence evolution at different stages during the plating/stripping process. The results agree well with the changes in cell overpotential, suggesting that electrochemically derived interface evolution enables the formation of a robust and stable Li/$LPSCl_{0.3}F_{0.7}$ interface. The Li plating/stripping behavior at 1.27 mA cm^{-2} and 1 mAh cm^{-2} is displayed in Figure 2b. The symmetric cell undergoes an initial activation process similar to that of the cells cycled at 0.127 mA cm^{-2}: the overpotential increases from ∼220 to ∼350 mV in the initial 100 h, followed by a stable overpotential that is maintained at ∼150 mV after 1000 h. More remarkably, when we increased the current density and cutoff capacity to 6.37 mA cm^{-2} and 5 mAh cm^{-2}, respectively, for the cycled symmetric cell, the cell can continue performing ultrastable Li plating/stripping for an additional 250 h (Figure 2c). The magnified polarization curves of Li plating/stripping are shown in Figure S7, suggesting a typically featured Li nucleation and growth process at such a high current density and cutoff capacity. To the best of our knowledge, the presented Li//$LPSCl_{0.3}F_{0.7}$//Li symmetric cell performance has surpassed any other reported performance with various sulfide SSEs at RT and can be comparable to the best performance in liquid electrolyte systems without using Li metals designed in a complicated manner (see the performance comparison in Table S1).

To understand the reason behind the high performance of Li//$LPSCl_{0.3}F_{0.7}$//Li symmetric cells, several characterizations were carried out. First, rest time-resolved EIS of the fabricated

https://dx.doi.org/10.1021/acsenergylett.0c00207
ACS Energy Lett. 2020, 5, 1035−1043

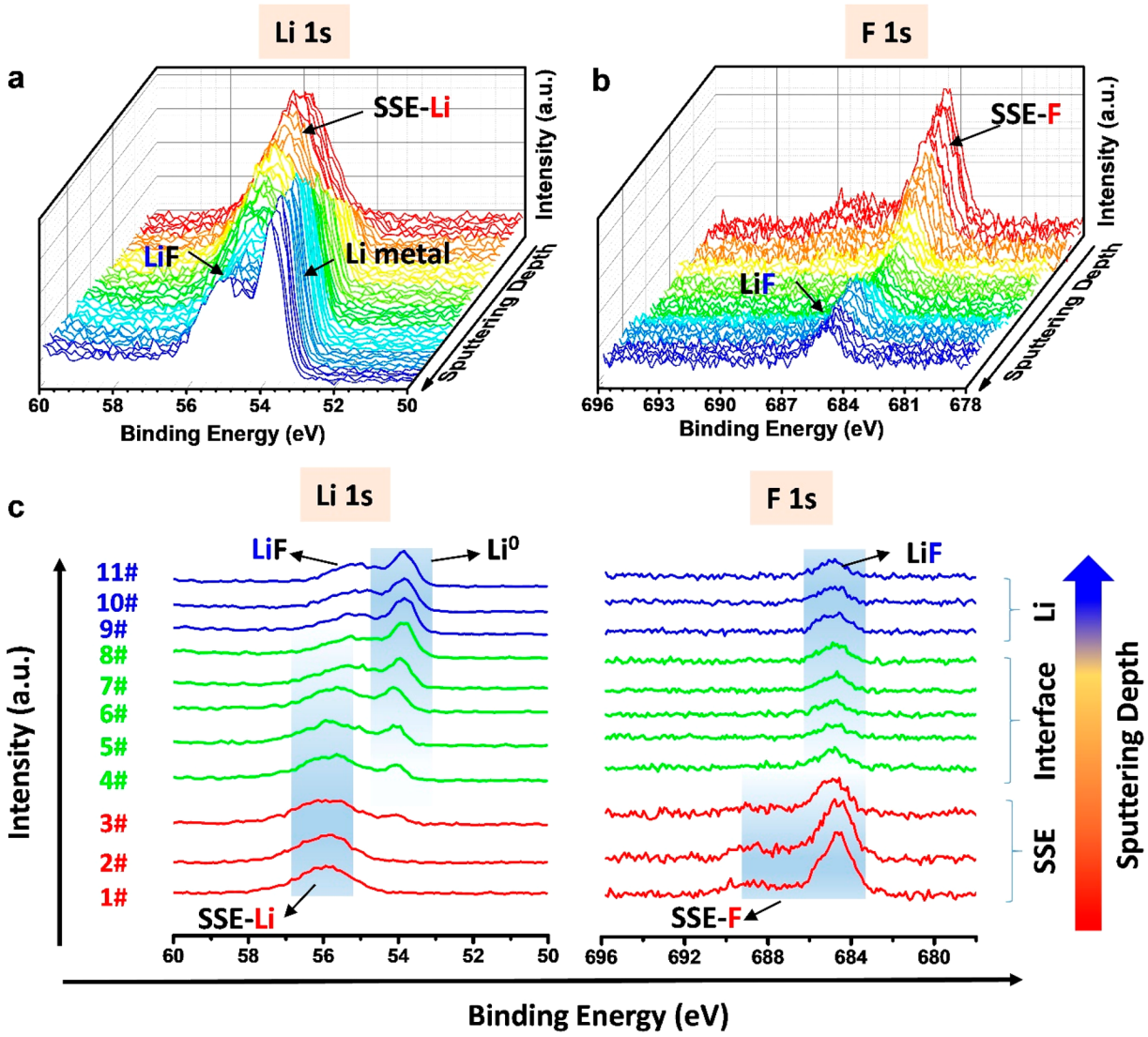

Figure 4. XPS depth profiling analysis of the Li metal/SSE interface. (a and b) Overall evolution of the Li 1s and F 1s spectra with sputtering depth at the Li/LPSCl$_{0.3}$F$_{0.7}$ interface. (c) Representative Li 1s and F 1s XPS spectra extracted from panels a and b.

Li//LPSCl$_{0.3}$F$_{0.7}$//Li symmetric cell (Figure S8) verifies that the Li/LPSCl$_{0.3}$F$_{0.7}$ interface is chemically stable, due to the negligible change in interface impedance over 24 h. Then, SEM was used to examine the difference in morphology between LPSCl and LPSCl$_{0.3}$F$_{0.7}$ electrolyte pellets made through cold pressing before electrochemical cycling. Figure S9a suggests that there is a large area of cracks on the surface of the LPSCl pellet. These gaps would provide space for Li dendrite growth and thus easily cause short circuits.[38] By contrast, the surface of the LPSCl$_{0.3}$F$_{0.7}$ pellet (Figure S9b) is much denser and relatively smoother, resulting from the good densification ability of the LPSCl$_{0.3}$F$_{0.7}$ electrolyte derived from effective fluorination. For the LPSCl$_{0.3}$F$_{0.7}$ SSE with F incorporated, the bonding energy of P−S is reduced, while the free volume of the SSE would increase to decrease Young's modulus.[39] The lower bonding energy and Young's modulus can result in an increase in relative density for enhanced densification ability of the electrolyte.[39] In addition to the potentially improved mechanical property of the fluorinated LPSCl$_{0.3}$F$_{0.7}$ sulfide SSE, the in situ-formed functional Li/LPSCl$_{0.3}$F$_{0.7}$ interface is confirmed by using various characterizations. Ex situ SEM measurements were conducted to study the morphology of the Li metal surface after Li plating/stripping for ∼200 h (0.127 mA cm^{-2} and 0.1 mAh cm^{-2}) in the Li//LPSCl$_{0.3}$F$_{0.7}$//Li symmetric cell (which underwent activation). As suggested in Figure 3a-1, the Li surface after Li plating/stripping is very smooth. Close observation (Figure 3a-2) suggests that numerous nanosheets are present on the consecutive and homogeneous surface. The side-view SEM images of the Li metal layer (Figure S10) also suggest the formation of a sheetlike coating on the Li metal surface. However, obvious corrosion reactions occur on the Li/LPSCl interface (Li plating/stripping for ∼20 h) as suggested in Figure S11a. The black spots in Figure S10b indicate lithium dendrite growth from these sites. Side-view SEM images of the Li metal surface (obtained after the short circuit happens to the Li//LPSCl//Li symmetric cell) can also reveal the formation of Li dendrites (Figure S11c,d). Time-of-flight secondary-ion mass spectrometry (ToF-SIMS) was used to analyze the surface chemical species on the cycled Li metal electrode with ion milling depth profiling. For an analysis area of 500 μm × 500 μm, before Cs$^+$-ion sputtering, the obtained

https://dx.doi.org/10.1021/acsenergylett.0c00207
ACS Energy Lett. 2020, 5, 1035−1043

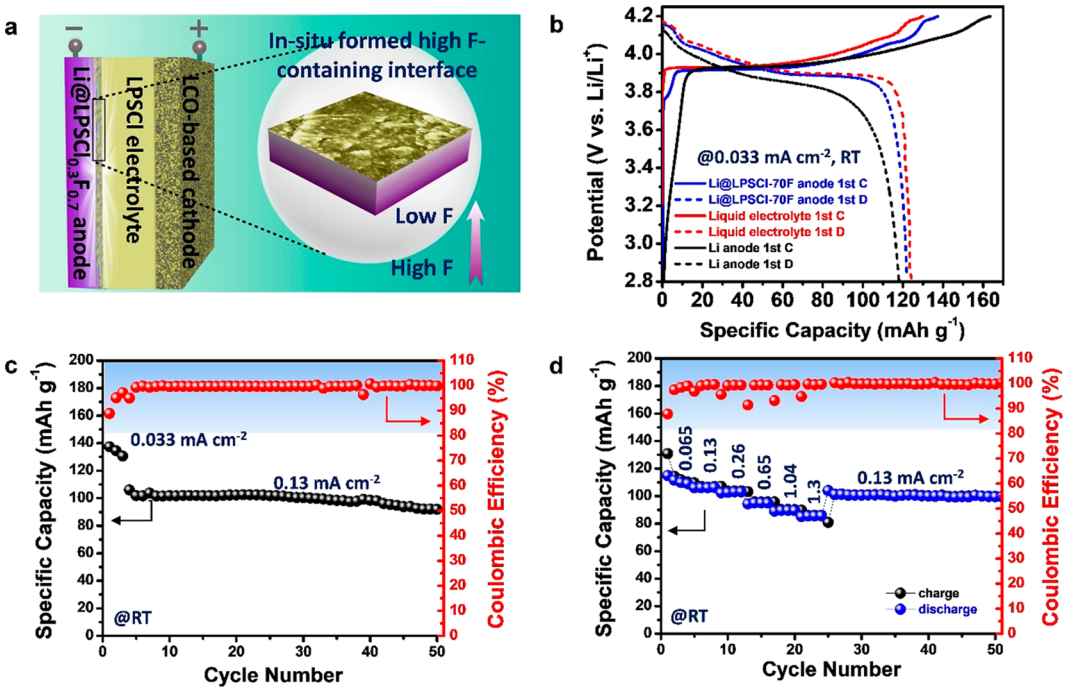

Figure 5. Electrochemical performance of ASSLMBs. (a) Schematic diagram of the Li@LPSCl$_{0.3}$F$_{0.7}$//LPSCl//LCO@LNO/LPSCl ASSLMBs with the highlighted fluorinated interface layer. (b) Charge−discharge profiles of the fabricated ASSLMBs. (c) Cycling stability of the Li@LPSCl$_{0.3}$F$_{0.7}$//LPSCl//LCO@LNO/LPSCl ASSLBs at RT. (d) Rate capability of the Li@LPSCl$_{0.3}$F$_{0.7}$//LPSCl//LCO@LNO/LPSCl ASSLBs at RT.

chemical species mapping suggests Li, F, P, S, and Cl species disperse uniformly on the Li metal surface (Figure S12). Along with Cs^+-ion sputtering, ToF-SIMS depth profiles are shown in Figure 3b.The increasing count intensity of Li suggests the detection depth is gradually approaching the Li metal surface. Obviously, the intensity of P, S, and Cl species decreases with this increased probing depth. It is interesting to note that the maximum F intensity was observed before the Li metal surface was reached, which suggests the F species have a gradient dispersed in the direction perpendicular to the Li metal surface. A series of chemical species images recorded after Cs^+-ion sputtering are shown in Figure 3c. The spatially different dispersion of Li-, F-, P-, S-, and Cl-containing species derived from gradient differences can also be observed directly.

XPS depth profiling analysis was further conducted to study the chemical composition of the Li/LPSCl$_{0.3}$F$_{0.7}$ interface (after precycling for ∼200 h in the Li//LPSCl$_{0.3}$F$_{0.7}$//Li symmetric cell at 0.127 mA cm^{-2} and 0.1 mAh cm^{-2}). Multiple signal collections (50 times in total) were conducted after sputtering with the Ar500+ cluster ion source for 30 min at intervals. The overall evolution of the P 2p, S 2p, and Cl 2p spectra from the Li@LPSCl$_{0.3}$F$_{0.7}$ surface to the Li metal is present in Figure S13. Along with the sputtering depth increasing, signal intensities gradually decrease and nearly reach zero toward the end of the testing period, suggesting that depth profiling successfully penetrated through the interface layer to the Li metal layer. The evolution of the Li 1s and F 1s spectra is studied in detail as displayed in panels a and b of Figure 4, respectively. Representative Li 1s and F 1s spectra in different layers of interest are extracted and summarized as shown in Figure 4c. The spectra of 1#−3# are assigned to the SSE layer. The intensity of both Li 1s and F 1s in this layer tends to decrease when progressing toward the interface. No binding energy shift is observed in the characteristic peaks of each element, indicating the peripheral LPSCl$_{0.3}$F$_{0.7}$ SSE is stable against Li metal. In the interface layer (4#−8#), for Li 1s spectra, the intensities of peaks at ∼55.9 eV assigned to the Li 1s in the LPSCl$_{0.3}$F$_{0.7}$ electrolyte decrease along with an increasing sputtering depth, which accompanies the increase in the intensity of the elemental Li (Li^0) peak at ∼53.9 eV.[17,40] One small peak at ∼55.1 eV starts to occur at the place that is very close to the Li metal and even in the Li metal layer, which is related to the strong electronegativity of F toward Li in LiF compounds. F 1s spectra at the interface show a different evolution trend compared with that of Li 1s spectra. The dominant F species at the interface is from Li−F bonds (indexed at ∼684.8 eV).[19] The intensity of Li−F (from LPSCl$_{0.3}$F$_{0.7}$ SSEs) decreases in the initial achievement of the interface layer because of the vanishing LPSCl$_{0.3}$F$_{0.7}$ SSEs, while an increase in the deeper interface closer to the Li metal results from the gradual formation of LiF compounds. This result agrees well with the ToF-SIMS result as shown in panels b and c of Figure 3. In short, the effective LiF-containing interface was formed through the interface and the closed Li metal layer, serving as the robust protection layer for the observed ultrastable Li plating/stripping.

Overall, the smooth interphase of Li/LPSCl$_{0.3}$F$_{0.7}$ with a dense and sheetlike morphology is formed in situ after the initial activation process. Moreover, the fluorinated LPSCl$_{0.3}$F$_{0.7}$ electrolyte can support the formation of a robust fluorinated interface (rich LiF). Also, the self-healing feature of this interface layer guarantees long-term protection. All these morphology and physicochemical properties have been demonstrated to play very important roles in preventing Li dendrite formation and stabilize the interface between Li metal and sulfide electrolytes.

To demonstrate the application potential of the stabilized Li metal interface with a high degree of fluorination, sulfide-based

https://dx.doi.org/10.1021/acsenergylett.0c00207
ACS Energy Lett. 2020, 5, 1035−1043

ASSLMBs are constructed by using $LPSCl_{0.3}F_{0.7}$ pretreated Li metal (plating/stripping for ~200 h at 0.127 mA cm^{-2} and 0.1 mAh cm^{-2}) as the anode (Li@$LPSCl_{0.3}F_{0.7}$), $LiCoO_2$ (LCO) with a $LiNbO_x$ (LNO) protection coating layer combined with LPSCl as the cathode composite (LCO@LNO/LPSCl), and LPSCl as the electrolyte (Figure 5a). The loading mass of the LCO cathode is ~8.92 mg cm^{-2}. SEM images and EDX element mapping of the cross section of this full battery are presented in Figure S14, indicating good contacts between the Li@$LPSCl_{0.3}F_{0.7}$ anode and LPSCl SSEs as well as within the cathode layer. RT galvanostatic charge and discharge experiments were conducted in the voltage range of 2.8−4.2 V (vs Li/Li^+). The charge and discharge curve obtained at a low current density of 0.033 mA cm^{-2} (1 C corresponds to 1.3 mA cm^{-2}) is shown as the blue curve in Figure 5b, which is extremely similar to the red curve that was obtained in the liquid electrolyte-based coin cell (Li//liquid electrolyte//LCO). This indicates a smooth electrochemical reaction takes place in the solid state. In addition, no obvious voltage plateau/slope corresponding to the side reaction on the cathode or anode is found during the charge and discharge process of Li@$LPSCl_{0.3}F_{0.7}$//LPSCl//LCO@LNO/LPSCl ASSLMBs, with the exception of the somewhat inevitable space charge effect indicated by a small slope before the charging plateau of 3.9 V is reached.[41] Similar to the capacity and high reversibility delivered in the Li//liquid electrolyte//LCO battery, the first discharge specific capacity is ≤122 mAh g^{-1} and a high Coulombic efficiency of 89% can be achieved in the Li@$LPSCl_{0.3}F_{0.7}$//LPSCl//LCO@LNO/LPSCl battery. By contrast, if the Li metal is used without $LPSCl_{0.3}F_{0.7}$ pretreatment as the anode, the Li//LPSCl//LCO@LNO/LPSCl ASSLMBs present very poor electrochemical performance (black charge and discharge curves in Figure 5b). Side reactions take place severely at the Li/LPSCl interface, leading to a large irreversible capacity. The RT cycling stability of the Li@$LPSCl_{0.3}F_{0.7}$//LPSCl//LCO@LNO/LPSCl battery is shown in Figure 5c; after the initial cycling at a low current density of 0.033 mA cm^{-2}, the battery operates smoothly at 0.13 mA cm^{-2}. The specific discharge capacity remains stable during the first 40 cycles with an ultrahigh Coulombic efficiency (>99.5%), and capacity retention stands at 95% after 50 cycles. The problems associated with the Li anode/sulfide electrolyte interface (interfacial side reactions and Li dendrite formation) would be much more serious under high current densities,[42] while the Li/$LPSCl_{0.3}F_{0.7}$//LPSCl//LCO@LNO/LPSCl battery can show an excellent rate capability at RT. As suggested in Figure 5d, the specific capacity stands at 118 mAh g^{-1} under a low current density of 0.065 mA cm^{-2}, while the specific capacity can reach 115, 103, 95, 89, and 86 mAh g^{-1} at increased current densities of 0.13, 0.26, 0.65, 1.04, and 1.3 mA cm^{-2}, respectively. Furthermore, the specific capacity can recover to 101 mAh g^{-1} and remain stable, when the current density declines to 0.13 mA cm^{-2}. These results prove the performance of our full cells is one of the best in the reported sulfide-based ASSLMBs (see the performance comparison in Table S2). In stark contrast to the excellent electrochemical performance of the sulfide-based ASSLMBs employing Li@$LPSCl_{0.3}F_{0.7}$ as the anode, Li//LPSCl//LCO@LNO/LPSCl full batteries that use bare Li as the anode cannot even operate under a current density of 0.13 mA cm^{-2} when the cycling number is extended (Figure S15). The battery has difficulty in charging and delivers a very large but false specific charge capacity, which is ascribed to the unstable Li/LPSCl interface and the resultant degradation of LPSCl electrolytes.

In conclusion, F is incorporated into the popular Argyrodite Li_6LP_5Cl sulfide-based electrolytes for the first time via conventional solid-state synthesis routes. We have verified that the fluorinated $LPSCl_{0.3}F_{0.7}$ electrolyte exhibits an outstanding stability toward Li metal during Li plating/stripping. In the Li//$LPSCl_{0.3}F_{0.7}$//Li symmetric cell, stable Li plating/stripping for >1000 h can be achieved at a current density of 1.27 mA cm^{-2} and a capacity of 1 mAh cm^{-2}. Even under a rarely reported current density of 6.37 mA cm^{-2} and a capacity of 5 mAh cm^{-2}, the Li//$LPSCl_{0.3}F_{0.7}$//Li symmetric cell can still display stable Li plating/stripping for >250 h. Furthermore, the excellent Li metal interface can be applied to realize the high performance in Li@$LPSCl_{0.3}F_{0.7}$//LPSCl//LCO@LNO/LPSCl full batteries. The superior in situ-formed interface between the Li metal and $LPSCl_{0.3}F_{0.7}$ is demonstrated to be endowed with a highly dense and sheetlike surface morphology, as well as a high concentration of LiF compounds. The fluorinated sulfide SSE can induce the formation of an ultrastable Li metal interface and is expected to lead to significant steps toward the development of high-performance ASSLMBs.

■ ASSOCIATED CONTENT

Supporting Information

The Supporting Information is available free of charge at https://pubs.acs.org/doi/10.1021/acsenergylett.0c00207.

Experimental section, magnified regions of the XRD patterns, supplemental XPS results, Raman spectra, impedance plots, DC polarization curves, SEM characterizations, ToF-SIMS chemical images, electrochemical performance, and summarized tables for making comparisons (PDF)

■ AUTHOR INFORMATION

Corresponding Author

Xueliang Sun − *Department of Mechanical and Materials Engineering, University of Western Ontario, London, Ontario N6A 5B9, Canada;* orcid.org/0000-0003-0374-1245; Email: xsun9@uwo.ca

Authors

Feipeng Zhao − *Department of Mechanical and Materials Engineering, University of Western Ontario, London, Ontario N6A 5B9, Canada*

Qian Sun − *Department of Mechanical and Materials Engineering, University of Western Ontario, London, Ontario N6A 5B9, Canada*

Chuang Yu − *Department of Mechanical and Materials Engineering, University of Western Ontario, London, Ontario N6A 5B9, Canada*

Shumin Zhang − *Department of Mechanical and Materials Engineering, University of Western Ontario, London, Ontario N6A 5B9, Canada*

Keegan Adair − *Department of Mechanical and Materials Engineering, University of Western Ontario, London, Ontario N6A 5B9, Canada*

Sizhe Wang − *Department of Mechanical and Materials Engineering, University of Western Ontario, London, Ontario N6A 5B9, Canada*

Yulong Liu − *Department of Mechanical and Materials Engineering, University of Western Ontario, London, Ontario N6A 5B9, Canada*
Yang Zhao − *Department of Mechanical and Materials Engineering, University of Western Ontario, London, Ontario N6A 5B9, Canada*
Jianwen Liang − *Department of Mechanical and Materials Engineering, University of Western Ontario, London, Ontario N6A 5B9, Canada*
Changhong Wang − *Department of Mechanical and Materials Engineering, University of Western Ontario, London, Ontario N6A 5B9, Canada*
Xiaona Li − *Department of Mechanical and Materials Engineering, University of Western Ontario, London, Ontario N6A 5B9, Canada*
Xia Li − *Department of Mechanical and Materials Engineering, University of Western Ontario, London, Ontario N6A 5B9, Canada*
Wei Xia − *Department of Mechanical and Materials Engineering, University of Western Ontario, London, Ontario N6A 5B9, Canada; Academy for Advanced Interdisciplinary Studies, Southern University of Sciences and Technology, Shenzhen 518000, P. R. China*
Ruying Li − *Department of Mechanical and Materials Engineering, University of Western Ontario, London, Ontario N6A 5B9, Canada*
Huan Huang − *Glabat Solid-State Battery Inc., London, Ontario N6G 4X8, Canada*
Li Zhang − *China Automotive Battery Research Institute Company, Ltd, Beijing 100088, P. R. China*
Shangqian Zhao − *China Automotive Battery Research Institute Company, Ltd, Beijing 100088, P. R. China*
Shigang Lu − *China Automotive Battery Research Institute Company, Ltd, Beijing 100088, P. R. China*

Complete contact information is available at:
https://pubs.acs.org/10.1021/acsenergylett.0c00207

Author Contributions

F.Z. and X.S. conceived the project and designed the experiments. F.Z., C.Y., and S. Zhang conducted material synthesis and electrochemical measurements. F.Z. and Q.S. carried out XRD measurement and analysis. Q.S., J.L., and C.W. helped with the analysis of XPS data. Q.S. and J.L. helped with the electronic conductivity measurements. S.W. drew the schematic diagram. Y.L., Xia Li, and R.L. helped with the SEM and EDX analysis. Y.Z. and K.A. participated in the discussion of ToF-SIMS data. J.L. helped to carry out the Raman measurements. Y.Z. and Xiaona Li helped to analyze the cell performance. W.X., H.H., L.Z., S. Zhao, and S.L. discussed the data. F.Z. wrote the manuscript. K.A. polished the writing. All of the authors discussed the results and commented on the manuscript.

Notes

The authors declare no competing financial interest.

■ ACKNOWLEDGMENTS

This research was supported by the Natural Sciences and Engineering Research Council of Canada (NSERC), the Canada Research Chair Program (CRC), the Canada Foundation for Innovation (CFI), the Ontario Research Foundation (ORF), China Automotive Battery Research Institute Co., Ltd., Glabat Solid-State Battery Inc., and the University of Western Ontario (UWO). The authors gratefully acknowledge Dr. Mark Biesinger and Dr. Heng-Yong Nie for their kind help with the test and analysis of XPS and ToF-SIMS at Surface Science Western (Western University).

■ REFERENCES

(1) Manthiram, A.; Yu, X.; Wang, S. Lithium battery chemistries enabled by solid-state electrolytes. *Nat. Rev. Mater.* **2017**, *2*, 16103.
(2) Xin, S.; You, Y.; Wang, S.; Gao, H.-C.; Yin, Y.-X.; Guo, Y.-G. Solid-State Lithium Metal Batteries Promoted by Nanotechnology: Progress and Prospects. *ACS Energy Lett.* **2017**, *2*, 1385−1394.
(3) Chen, R.; Li, Q.; Yu, X.; Chen, L.; Li, H. Approaching Practically Accessible Solid-State Batteries: Stability Issues Related to Solid Electrolytes and Interfaces. *Chem. Rev.* **2019**, DOI: 10.1021/acs.chemrev.9b00268.
(4) Quartarone, E.; Mustarelli, P. Electrolytes for solid-state lithium rechargeable batteries: recent advances and perspectives. *Chem. Soc. Rev.* **2011**, *40*, 2525−2540.
(5) Zhang, Z.; Shao, Y.; Lotsch, B.; Hu, Y.-S.; Li, H.; Janek, J.; Nazar, L. F.; Nan, C.-W.; Maier, J.; Armand, M.; Chen, L. New horizons for inorganic solid state ion conductors. *Energy Environ. Sci.* **2018**, *11*, 1945−1976.
(6) Fan, L.; Wei, S.; Li, S.; Li, Q.; Lu, Y. Recent Progress of the Solid-State Electrolytes for High-Energy Metal-Based Batteries. *Adv. Energy Mater.* **2018**, *8*, 1702657.
(7) Gao, Z.; Sun, H.; Fu, L.; Ye, F.; Zhang, Y.; Luo, W.; Huang, Y. Promises, Challenges, and Recent Progress of Inorganic Solid-State Electrolytes for All-Solid-State Lithium Batteries. *Adv. Mater.* **2018**, *30*, 1705702.
(8) Kato, Y.; Hori, S.; Saito, T.; Suzuki, K.; Hirayama, M.; Mitsui, A.; Yonemura, M.; Iba, H.; Kanno, R. High-power all-solid-state batteries using sulfide superionic conductors. *Nat. Energy* **2016**, *1*, 16030.
(9) Kamaya, N.; Homma, K.; Yamakawa, Y.; Hirayama, M.; Kanno, R.; Yonemura, M.; Kamiyama, T.; Kato, Y.; Hama, S.; Kawamoto, K.; Mitsui, A. A lithium superionic conductor. *Nat. Mater.* **2011**, *10*, 682−686.
(10) Lee, H.; Oh, P.; Kim, J.; Cha, H.; Chae, S.; Lee, S.; Cho, J. Advances and Prospects of Sulfide All-Solid-State Lithium Batteries via One-to-One Comparison with Conventional Liquid Lithium Ion Batteries. *Adv. Mater.* **2019**, *31*, 1900376.
(11) Zhang, Q.; Cao, D.; Ma, Y.; Natan, A.; Aurora, P.; Zhu, H. Sulfide-Based Solid-State Electrolytes: Synthesis, Stability, and Potential for All-Solid-State Batteries. *Adv. Mater.* **2019**, *31*, 1901131.
(12) Xu, L.; Tang, S.; Cheng, Y.; Wang, K. Y.; Liang, J. Y.; Liu, C.; Cao, Y. C.; Wei, F.; Mai, L. Q. Interfaces in Solid-State Lithium Batteries. *Joule* **2018**, *2*, 1991−2015.
(13) Wenzel, S.; Leichtweiss, T.; Krüger, D.; Sann, J.; Janek, J. Interphase formation on lithium solid electrolytes—An in situ approach to study interfacial reactions by photoelectron spectroscopy. *Solid State Ionics* **2015**, *278*, 98−105.
(14) Zhu, Y.; He, X.; Mo, Y. First principles study on electrochemical and chemical stability of solid electrolyte−electrode interfaces in all-solid-state Li-ion batteries. *J. Mater. Chem. A* **2016**, *4*, 3253−3266.
(15) Kobayashi, T.; Yamada, A.; Kanno, R. Interfacial reactions at electrode/electrolyte boundary in all solid-state lithium battery using inorganic solid electrolyte, thio-LISICON. *Electrochim. Acta* **2008**, *53*, 5045−5050.
(16) Kato, A.; Kowada, H.; Deguchi, M.; Hotehama, C.; Hayashi, A.; Tatsumisago, M. XPS and SEM analysis between Li/Li 3 PS 4 interface with Au thin film for all-solid-state lithium batteries. *Solid State Ionics* **2018**, *322*, 1−4.
(17) Gao, Y.; Wang, D. W.; Li, Y. G. C.; Yu, Z. X.; Mallouk, T. E.; Wang, D. H. Salt-Based Organic-Inorganic Nanocomposites: Towards A Stable Lithium Metal/Li10GeP2S12 Solid Electrolyte Interface. *Angew. Chem., Int. Ed.* **2018**, *57*, 13608−13612.

(18) Xu, R.; Han, F.; Ji, X.; Fan, X.; Tu, J.; Wang, C. Interface engineering of sulfide electrolytes for all-solid-state lithium batteries. *Nano Energy* **2018**, *53*, 958−966.
(19) Fan, X.; Ji, X.; Han, F.; Yue, J.; Chen, J.; Chen, L.; Deng, T.; Jiang, J.; Wang, C. Fluorinated solid electrolyte interphase enables highly reversible solid-state Li metal battery. *Sci. Adv.* **2018**, *4*, eaau9245.
(20) Wen, J. Y.; Huang, Y.; Duan, J.; Wu, Y. M.; Luo, W.; Zhou, L. H.; Hu, C. C.; Huang, L. Q.; Zheng, X. Y.; Yang, W. J.; Wen, Z. Y.; Huang, Y. H. Highly Adhesive Li-BN Nanosheet Composite Anode with Excellent Interfacial Compatibility for Solid-State Li Metal Batteries. *ACS Nano* **2019**, *13*, 14549−14556.
(21) Han, F.; Yue, J.; Zhu, X.; Wang, C. Suppressing Li Dendrite Formation in Li2S-P2S5 Solid Electrolyte by LiI Incorporation. *Adv. Energy Mater.* **2018**, *8*, 1703644.
(22) Albertus, P.; Babinec, S.; Litzelman, S.; Newman, A. Status and challenges in enabling the lithium metal electrode for high-energy and low-cost rechargeable batteries. *Nat. Energy* **2018**, *3*, 16−21.
(23) Zhang, Q. Fluorinated interphases. *Nat. Nanotechnol.* **2018**, *13*, 623−624.
(24) Wang, C.; Meng, Y. S.; Xu, K. Perspective—Fluorinating Interphases. *J. Electrochem. Soc.* **2019**, *166*, A5184−A5186.
(25) von Aspern, N.; Roschenthaler, G. V.; Winter, M.; Cekic-Laskovic, I. Fluorine and Lithium: Ideal Partners for High-Performance Rechargeable Battery Electrolytes. *Angew. Chem., Int. Ed.* **2019**, *58*, 15978−16000.
(26) Li, T.; Zhang, X.-Q.; Shi, P.; Zhang, Q. Fluorinated Solid-Electrolyte Interphase in High-Voltage Lithium Metal Batteries. *Joule* **2019**, *3*, 2647−2661.
(27) He, M.; Guo, R.; Hobold, G. M.; Gao, H.; Gallant, B. M. The intrinsic behavior of lithium fluoride in solid electrolyte interphases on lithium. *Proc. Natl. Acad. Sci. U. S. A.* **2020**, *117*, 73−79.
(28) Xu, R.; Cheng, X.-B.; Yan, C.; Zhang, X.-Q.; Xiao, Y.; Zhao, C.-Z.; Huang, J.-Q.; Zhang, Q. Artificial Interphases for Highly Stable Lithium Metal Anode. *Matter* **2019**, *1*, 317−344.
(29) Yu, C.; van Eijck, L.; Ganapathy, S.; Wagemaker, M. Synthesis, structure and electrochemical performance of the argyrodite Li 6 PS 5 Cl solid electrolyte for Li-ion solid state batteries. *Electrochim. Acta* **2016**, *215*, 93−99.
(30) Mo, F.; Ruan, J.; Sun, S.; Lian, Z.; Yang, S.; Yue, X.; Song, Y.; Zhou, Y.; Fang, F.; Sun, G.; Peng, S.; Sun, D. Inside or Outside: Origin of Lithium Dendrite Formation of All Solid-State Electrolytes. *Adv. Energy Mater.* **2019**, *9*, 1902123.
(31) Dietrich, C.; Koerver, R.; Gaultois, M. W.; Kieslich, G.; Cibin, G.; Janek, J.; Zeier, W. G. Spectroscopic characterization of lithium thiophosphates by XPS and XAS - a model to help monitor interfacial reactions in all-solid-state batteries. *Phys. Chem. Chem. Phys.* **2018**, *20*, 20088−20095.
(32) Deiseroth, H. J.; Kong, S. T.; Eckert, H.; Vannahme, J.; Reiner, C.; Zaiss, T.; Schlosser, M. Li6PS5X: a class of crystalline Li-rich solids with an unusually high Li+ mobility. *Angew. Chem., Int. Ed.* **2008**, *47*, 755−758.
(33) Yubuchi, S.; Teragawa, S.; Aso, K.; Tadanaga, K.; Hayashi, A.; Tatsumisago, M. Preparation of high lithium-ion conducting Li6PS5Cl solid electrolyte from ethanol solution for all-solid-state lithium batteries. *J. Power Sources* **2015**, *293*, 941−945.
(34) Zhang, Z.; Zhang, L.; Liu, Y.; Yu, C.; Yan, X.; Xu, B.; Wang, L.-m. Synthesis and characterization of argyrodite solid electrolytes for all-solid-state Li-ion batteries. *J. Alloys Compd.* **2018**, *747*, 227−235.
(35) Wang, S.; Zhang, Y.; Zhang, X.; Liu, T.; Lin, Y.-H.; Shen, Y.; Li, L.; Nan, C.-W. High-Conductivity Argyrodite Li6PS5Cl Solid Electrolytes Prepared via Optimized Sintering Processes for All-Solid-State Lithium−Sulfur Batteries. *ACS Appl. Mater. Interfaces* **2018**, *10*, 42279−42285.
(36) Han, F.; Westover, A.; Yue, J.; Fan, X.; Wang, F.; Chi, M.; Leonard, D.; Dudney, N.; Wang, H.; Wang, C. High electronic conductivity as the origin of lithium dendrite formation within solid electrolytes. *Nat. Energy* **2019**, *4*, 187−196.
(37) Wenzel, S.; Sedlmaier, S. J.; Dietrich, C.; Zeier, W. G.; Janek, J. Interfacial reactivity and interphase growth of argyrodite solid electrolytes at lithium metal electrodes. *Solid State Ionics* **2018**, *318*, 102−112.
(38) Nagao, M.; Hayashi, A.; Tatsumisago, M.; Kanetsuku, T.; Tsuda, T.; Kuwabata, S. In situ SEM study of a lithium deposition and dissolution mechanism in a bulk-type solid-state cell with a Li2S-P2S5 solid electrolyte. *Phys. Chem. Chem. Phys.* **2013**, *15*, 18600−18606.
(39) Kato, A.; Yamamoto, M.; Sakuda, A.; Hayashi, A.; Tatsumisago, M. Mechanical Properties of Li2S-P2S5 Glasses with Lithium Halides and Application in All-Solid-State Batteries. *ACS Appl. Energy Mater.* **2018**, *1*, 1002−1007.
(40) Huang, Y.; Chen, B.; Duan, J.; Yang, F.; Wang, T. R.; Wang, Z. F.; Yang, W. J.; Hu, C. C.; Luo, W.; Huang, Y. H. Graphitic Carbon Nitride (g-C3N4): An Interface Enabler for Solid-State Lithium Metal Batteries. *Angew. Chem., Int. Ed.* **2020**, *59*, 3699−3704.
(41) Haruyama, J.; Sodeyama, K.; Han, L. Y.; Takada, K.; Tateyama, Y. Space-Charge Layer Effect at Interface between Oxide Cathode and Sulfide Electrolyte in All-Solid-State Lithium-Ion Battery. *Chem. Mater.* **2014**, *26*, 4248−4255.
(42) Garcia-Mendez, R.; Mizuno, F.; Zhang, R.; Arthur, T. S.; Sakamoto, J. Effect of Processing Conditions of 75Li2S-25P2S5 Solid Electrolyte on its DC Electrochemical Behavior. *Electrochim. Acta* **2017**, *237*, 144−151.

https://dx.doi.org/10.1021/acsenergylett.0c00207
ACS Energy Lett. 2020, 5, 1035−1043